

Constraints on Earth's Core-Mantle boundary from nutation

J. Rekier^{1*}, S. A. Triana¹, A. Barik², D. Abdulah³, W. Kang³

¹Royal Observatory of Belgium, 3 avenue circulaire, 1180 Brussels, Belgium

²Johns Hopkins University, 3400 North Charles Street, Baltimore, MD 21218, USA

³Earth, Atmospheric and Planetary Science, Massachusetts Institute of Technology, USA

*Corresponding author. Email: jeremy.rekier@observatory.be.

July 14, 2025

Periodic variations in the Sun and Moon's gravitational pull cause small changes in Earth's rotational axis direction called nutation. Nutation components in the retrograde quasi-diurnal frequency band—measured in the terrestrial reference frame—are amplified by resonance with the Free Core Nutation (FCN), a rotational mode of Earth's fluid core¹. Dissipative processes at the core–mantle boundary (CMB) dampen this resonance, contributing to the observed phase lag between tidal forcing and Earth's rotational response². This phase lag is commonly attributed to electromagnetic (EM) coupling between the core and the electrically conducting lower mantle^{3;4;5}. However, estimates of mantle conductivity and radial magnetic field strength at the CMB suggest these effects are insufficient⁶. We show that the missing dissipation arises naturally from the excitation of internal waves in the fluid core by topographic features at

the CMB. Adapting a theoretical framework originally developed for tidal flow over oceanic topography^{7;8}, we compute the form drag and associated power flux induced by CMB topography. Our results are consistent with a CMB topography characterized by a root mean square amplitude of a few kilometers. The model favors weak stratification at the top of the core, though stronger stratification remains compatible with increased topographic amplitude. This mechanism provides independent constraints on CMB topography and stratification, complementing seismological and magnetic observations. Its generality offers a new framework for probing deep-interior dynamics across terrestrial planets.

Dissipative processes contribute to dampen the resonance of the Earth's nutation with the rotational mode known as the Free Core Nutation (FCN), causing the observed phase-lag between the tidal forcing and the Earth's response. Most of this occurs at the Core-Mantle Boundary (CMB), though some damping also occurs at the Inner-Core Boundary (ICB). Overall, this damping is relatively weak, measured with a quality factor at approximately^{9;10;11;12} $Q_{\text{FCN}} \approx 20,000 \pm 2500$, corresponding to a total dissipated power of¹³ $P \approx 9.5 \times 10^6 \text{ W}$. In current models, this value is attributed to Ohmic dissipation of electric currents induced in the core's conducting boundaries, a phenomenon referred to as Electromagnetic (EM) coupling^{3;4}. While the existence of these currents in the conducting inner core is hardly in doubt, their presence at the CMB is less certain due to the presumed low conductivity of the lower mantle¹⁴. It is customary to parametrize the torque produced by the core on the mantle with a single complex *coupling constant*, labeled K_{cmb} , with $\text{Re}(K_{\text{cmb}})$ proportional to the non-dissipative part of the torque, and $\text{Im}(K_{\text{cmb}})$ proportional to its dissipative part¹⁵. Based on the value of $\text{Im}(K_{\text{cmb}})$ inferred from observations, the dissipated power at the CMB amounts to $P \approx 8 \times 10^6 \text{ W}$ in physical units (see Methods).

We can compute the electromagnetic dissipation at the CMB using the theory of Mathews and Guo which also takes into account the much smaller contribution of viscous dissipation⁵. Setting the kinematic viscosity of the core to its estimated value for liquid iron,

$\nu = 10^{-6} \text{ m}^2/\text{s}$, the result depends on the conductivity of the core, which is usually taken as¹⁶ $\sigma_f = 5 \times 10^5 \text{ Sm}^{-1}$, and of the lower mantle, σ_m . It also depends on the radial magnetic field at the CMB, B_r , which is parametrized as the sum of a dipolar component, B_r^{dipolar} , which can be easily inferred from surface observation, as it is dominant, and a non-dipolar component^{4;6}, $B_r^{\text{non-dipolar}}$ which parametrizes the collective contribution of smaller scale components. Figure 1 gives a measure of the dissipation as a function of the radial magnetic field for three values of the mantle conductivity, with the core conductivity treated as an upper bound. We have used the `planetMagFields` software¹⁷ to obtain the dipolar and non-dipolar components of the magnetic field at the CMB from the 14th generation IGRF data¹⁸. We see that the EM coupling cannot fully account for the dissipation at the CMB, even assuming high lower mantle conductivity, and the discrepancy becomes even greater for lower conductivity values, favored by mineral physics studies¹⁴. An alternative dissipative mechanism is therefore desirable.

In oceans, tidal flows interacting with seafloor topography excite internal waves which transport momentum upward, dissipating a fraction of the tidal energy into the ocean, and driving bottom mixing^{8;7}. A similar process likely takes place at the Earth's CMB, where studies indicate the presence of a kilometer scale topography. In the Earth's core case, the tidal flow results from the differential rotation of the core relative to the mantle and has a (quasi) diurnal period. The oscillation of that flow over the topography excites internal waves within the core, that carry momentum away from the boundary, causing a pressure difference between the leading and the trailing sides of the topographic feature causing the excitation. This results in a net force, a *form drag*, aligned with the tidal flow velocity and proportional to its amplitude. At the global scale, this force, drag produces a torque on the mantle that dissipates a portion of the energy of the core differential rotation into the small scale internal waves (Figure 2).

The analogy between Earth's oceans and its liquid core is not new. Braginsky employed it perhaps most explicitly when he introduced the concept of the 'hidden Stratified Ocean of the

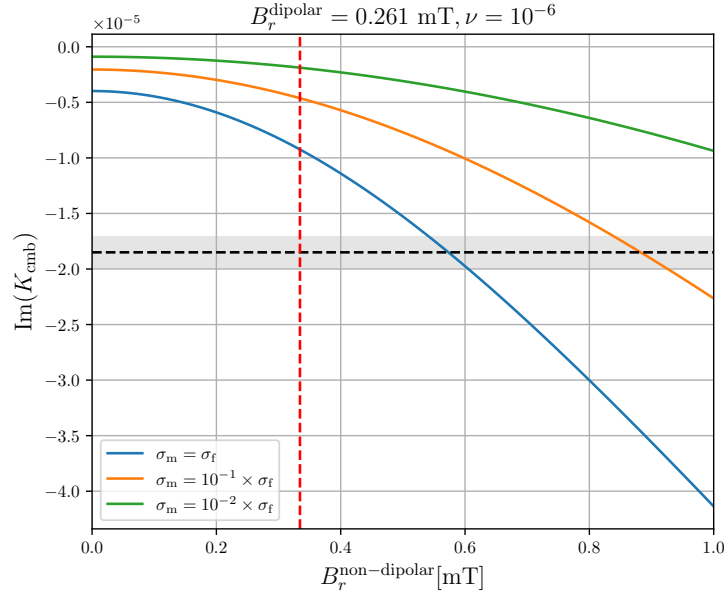


Figure 1: **Imaginary part of the coupling constant in the EM coupling scenario.** The colors correspond to 3 different values of the mantle conductivity. A rms value of 0.261 mT is assumed for the dipolar magnetic field. The vertical red line corresponds to a rms value of 0.334 mT for the non-dipolar part of the magnetic field inferred from the magnetic data. The dashed line corresponds to the value of $\text{Im}(K_{\text{cmb}})$ inferred from the nutation data with uncertainty represented by the shaded area.

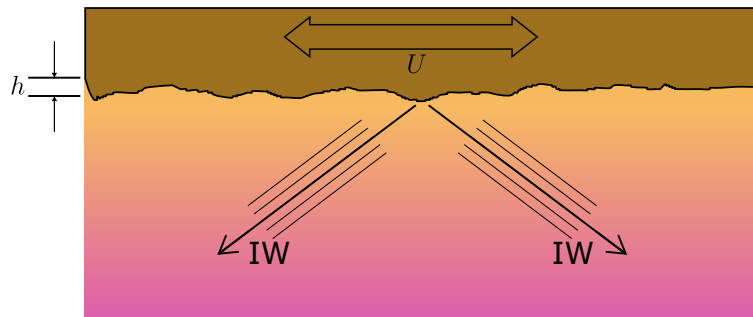


Figure 2: **Sketch of the internal waves excited by the topographic features of the Core-Mantle Boundary.** The nutation of the Earth's core produces a (quasi) diurnal tidal flow that interacts with the topography, exciting internal waves. These waves transport momentum which produces a periodic pressure drag on the surface and dissipates energy from the tidal flow.

Core’ (SOC)^{19;20}. The flow in this ‘hidden core ocean’ follows dynamical equations similar to those governing the flow at the bottom of the ocean. The existence of a stably stratified region at the top of the Earth’s core has been an object of debate for more than fifty years^{21;22}. There have been several estimates of the properties of this layer. Studies of geomagnetic secular variations^{23;24} suggest a thickness $d \approx 100 - 140$ km and a buoyancy frequency—a.k.a. *Brunt-Väisälä* frequency, N , of the order $N/\Omega \approx 1.5 - 2$, where $\Omega = 7.27 \times 10^{-5} \text{ s}^{-1}$ is the Earth’s spin rate^{19;24}. Seismic evidence^{25;26;27;28} suggests $d \approx 100 - 450$ km. Models of core thermodynamics and chemical barodiffusion^{29;30} point to a depth of the order $d \approx 100$ km with the frequency of $N/\Omega \approx 1.4 - 20$. A recent numerical model of core convection taking into account thermal heterogeneity at the CMB³¹ finds regional stratification on top of the Earth’s core with thickness of several hundred kilometers and $N/\Omega \approx 0.02 - 2$. Numerical models of the Earth’s geodynamo lean towards weaker stratification. Some models have suggested a stable layer with $d \approx 100$ km with a frequency of the order of the spin rate³², $N \approx \Omega$. More recent geodynamo simulations favor a very thin, weakly stratified layer, if one is present at all^{33;34}. We treat the degree of the density stratification as a free parameter in the present study.

Our knowledge of the CMB topography is currently very limited. Direct seismic measurements have large uncertainties and conclusions from various studies are not always compatible with each other. Notwithstanding, based on a review of current results, a typical topography amplitude of the order of a few km seems probable³⁵. This estimate also agrees well with simulated profiles of dynamic topography generated by mantle convection³⁶. To keep our model general, we adopt the following power spectrum for the CMB topography which has been shown to adequately capture the behavior of natural^{37;38;39} as well as synthetic surfaces^{40;41;42}:

$$|\hat{h}|^2 = \begin{cases} \frac{h_{\text{rms}}^2 \mathcal{H}}{k_0^2 \pi} \left(\frac{k}{k_0} \right)^{-2(\mathcal{H}+1)} & k \geq k_0, \\ 0 & k < k_0, \end{cases} \quad (1)$$

where \hat{h} denotes the Fourier transform of the topographic elevation function (see Supple-

mentary Information), k is the horizontal wave number, h_{rms} is the root mean square height, and \mathcal{H} is the *Hurst exponent* which characterizes the degree of self-similarity of the surface across length scales and is related to the fractal dimension⁴⁰. Values for natural surfaces are typically³⁸ $0.7 \leq \mathcal{H} \leq 0.9$, although values closer to $\mathcal{H} \approx 0.6$ are also possible³⁷. The last parameter, k_0 , is crucial. It sets the horizontal wavelength, $\lambda_0 = 2\pi/k_0$, above which the mantle topography ceases to be self-similar. In surfaces generated for industrial applications, this wavelength corresponds to the largest topographic feature⁴⁰. In this study, we interpret it as the largest horizontal wavelength that can efficiently excite internal waves.

To compute the total dissipated power and topographic torque at the CMB, and the resulting dissipation, we solve the local fluid dynamics equations at each latitude, ϑ , to obtain the pressure (form) drag and the associated power flux, then integrate over the CMB surface. Bell's original ocean model uses the *Traditional Approximation* (TA), which neglects the radial (locally vertical) component of the Coriolis force. This is valid at all latitudes only when buoyancy dominates over Coriolis effects (i.e., for large N). For small N , the TA breaks down near the equator. Since our analysis requires dissipation and form drag across all latitudes, we generalize the model beyond the TA. The outline of the derivation is given in the Methods, with full details in the Supplementary Information.

Figure 3 shows the power flux integrated over the CMB surface for representative values of the topographic parameters. The axis on the left gives the value in Watts with the corresponding value of $\text{Im}(K_{\text{cmb}})$ given on the right axis for convenience. The horizontal dashed line and gray area are reproduced from Fig. 1. We identify two regimes. For $N < \Omega$, the dissipation results from the excitation of *inertial waves*, the dynamics of which is dominated by the effect of the Coriolis force. For $N > \Omega$, the dissipation results from the excitation of *gravity waves*, the dynamics of which is dominated by the effect of buoyancy. Both types of waves become evanescent for $N = \Omega$ under the TA, as expected from the classic theory⁴³. Either type of waves can in principle generate the $P \approx 8 \times 10^6$ W of power needed to explain the dissipation of the nutation. Note, however, that our model treats N

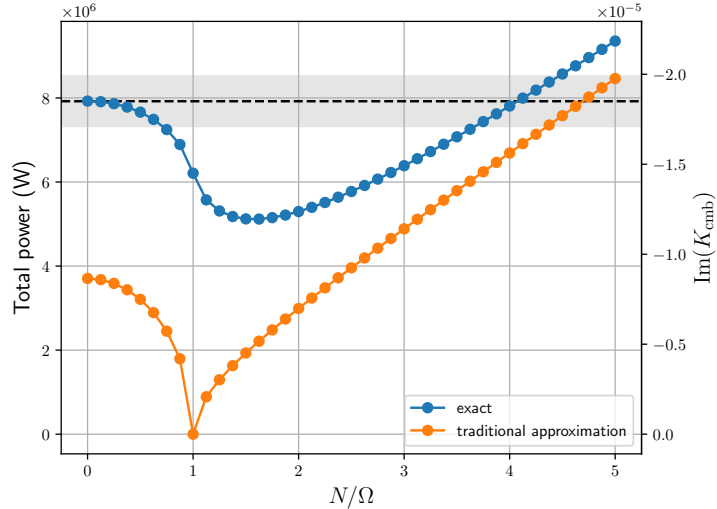


Figure 3: **Integrated power flux at the CMB for a representative topography, as a function of buoyancy** ($h_{\text{rms}} = 5.67 \text{ km}$, $\lambda_0 = 1000 \text{ km}$, and $\mathcal{H} = 0.7$). The orange and blue curves represent the solution with and without making the traditional approximation, respectively. The dashed line corresponds to the value of $\text{Im}(K_{\text{cmb}})$ inferred from the nutation data.

as a constant and does not take into account the finite depth of the stratified layer which is expected to greatly suppress the power flux⁴⁴. Our results for N large should therefore be treated as an upper bound and we conclude that the model favors a weakly stratified core.

Assuming a well-mixed outer core ($N = 0$), our results present a trade-off between the values of the parameters the r.m.s. amplitude of topography (h_{rms}), the characteristic topographic wavelength (λ_0), and the Hurst exponent (\mathcal{H}). Figure 4 gives the value of h_{rms} as a function of λ_0 for four values of \mathcal{H} . In all cases, the predicted amplitude is on the order of a few kilometers which matches estimations from seismology. The solid lines corresponds to the target dissipation of $P = 8 \times 10^6 \text{ W}$, with the uncertainties on that value represented by the shaded areas. In order to explain the observed dissipation, a larger wavelength can be compensated by a larger h_{rms} or a smaller \mathcal{H} .

As mentioned above, the form drag produced by the excitation of the internal waves is everywhere aligned with the tidal flow. This means that the resulting torque on the CMB is aligned with the angular velocity of the core. This contrasts with the torque computed

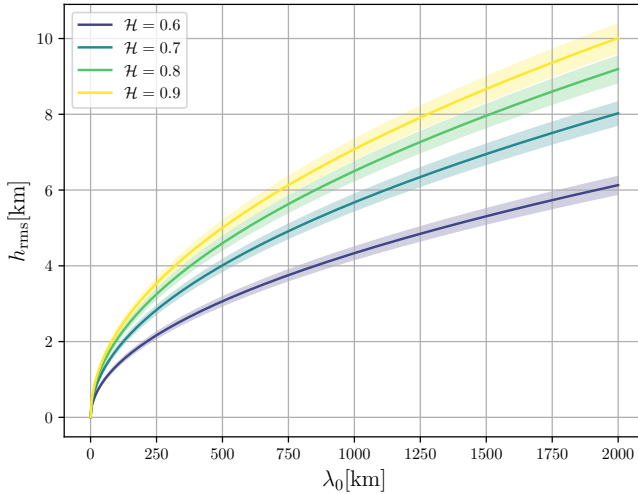


Figure 4: **Trade-off between the r.m.s. amplitude of the topography and the characteristic topographic wavelength for four values of the Hurst exponent.** In order to explain the observed dissipation, a larger wavelength must be compensated by a larger h_{rms} or a smaller \mathcal{H} . The solid lines corresponds to the target dissipation of $P = 8 \times 10^6$ W inferred from nutation data, with the uncertainties on that value represented by the shaded areas.

in the EM coupling theory which has an additional component perpendicular to the angular velocity. The latter causing no dissipation, its only effect is to slightly increase the frequency of the FCN by an amount written as the real part of the coupling constant, K_{cmb} . This quantity is not directly accessible from the nutations observations which can only provide a constraint on the combination $e_f + \text{Re}(K_{\text{cmb}})$, where e_f denotes the dynamical flattening of the core. The term e_f accounts for the pressure torque due to the ellipsoidal shape of the CMB. The theory presented here predicts: $\text{Re}(K_{\text{cmb}}) = 0$. Comparing with observations leads to an inferred $e_f = 2.67 \times 10^{-34;5}$, corresponding to a core flattening approximately 4.7% greater than the hydrostatic value¹², whereas the EM coupling theory predicting $\text{Re}(K_{\text{cmb}}) \approx 3 \times 10^{-5}$ requires a slightly smaller increase of approximately 3.6% compared to hydrostatic. Both cases can be accommodated with a modest increased of the polar flattening at the CMB of the order of a few hundred meters¹².

The results presented here demonstrate that internal waves excited by a CMB topography

with a root mean square amplitude of a few kilometers naturally explain the dissipation associated with the observed phase-lag in the nutations. The formalism works without appealing to a high conductivity of the lower mantle, contrary to the EM coupling theory. The new theory provides independent constraints on the CMB topography and density stratification which are compatible with previous seismic and geomagnetic data. With some modifications, the theory presented here can be used to investigate the effect of the inferred CMB topography on the variations in the length of day. The generality of the formalism makes it also applicable to investigate the variations of the rotation of other terrestrial planets. These investigations are currently being carried out by the authors.

Methods

The Free Core Nutation and its dissipation

The Free Core Nutation of the Earth is a free rotational mode with frequency⁴⁵:

$$\omega_{\text{fcn}} = -\Omega - \left(1 + \frac{A_f}{A_m}\right) \left(e_f - \beta + K_{\text{cmb}} + \frac{A_s}{A_f} K_{\text{icb}}\right) \Omega, \quad (2)$$

as measured in the terrestrial frame of reference. The symbols A_s , A_f , and A_m , represent the moments of inertia of the solid inner core, fluid outer core, and mantle, respectively. The FCN frequency is retrograde and quasi-diurnal, $\omega_{\text{fcn}} \approx -\Omega$, with a small correction given by the combination of terms enclosed in the second set of parentheses. Among these terms e_f parametrizes the flattening of the CMB, and β is a compliance parameter characterizing the elastic deformation properties of the mantle. The two remaining parameters, K_{cmb} and K_{icb} are complex valued. They parametrize the torque and the associated dissipation at the CMB, and at the ICB.

The kinetic energy of the FCN is due mostly to the uniform vorticity flow inside the core.

A very good approximation of the rate of energy dissipation is then¹³:

$$\frac{dE}{dt} = A_f |\boldsymbol{\omega}_f|^2 \text{Im}(\omega_{\text{fcn}}), \quad (3)$$

where $\boldsymbol{\omega}_f$ is the angular velocity of the core relative to the mantle. The theory of nutation gives² $|\boldsymbol{\omega}_f| \approx 2.4 \times 10^{-11} \text{ s}^{-1}$. By inserting Equation (2) into Equation (3), we obtain the sum of a term proportional to K_{cmb} , and one proportional to K_{icb} . The first of these corresponds to the dissipated power at the CMB:

$$P_{\text{cmb}} = -A_f \left(1 + \frac{A_f}{A_m}\right) \Omega |\boldsymbol{\omega}_f|^2 \text{Im}(K_{\text{cmb}}). \quad (4)$$

Injecting $A_f = 9.0583 \times 10^{36} \text{ kg m}^2$, and $A_m = 7.0996 \times 10^{37} \text{ kg m}^2$, gives $P_{\text{cmb}} \approx 8 \times 10^6 \text{ W}$, based on $\text{Im}(K_{\text{cmb}}) = -1.8 \times 10^{-5}$.

Outline of the torque and power computation

The detailed derivation of the formulas giving the torque and the integrated power flux at the CMB is given in the Supplementary Information (SI). For convenience, we here provide an outline of this derivation.

The tidal flow produced at a point of latitude, ϑ , and longitude φ , by a single retrograde nutation component of frequency ω_0 can be written as^{46;47}:

$$\mathbf{U} = U_0 \sin \vartheta \cos(\omega_0 t + \varphi) \hat{\mathbf{x}} - U_0 \sin(\omega_0 t + \varphi) \hat{\mathbf{y}}, \quad (5)$$

where $\hat{\mathbf{x}}$ is the unit vector pointing eastward along the zonal (a.k.a. azimuthal) direction, and $\hat{\mathbf{y}}$ is the unit vector pointing northward along the meridional direction. Bell^{7;8} first gave the expression for the secondary flow caused by the interaction of a tidal flow similar to Equation (5) with a rough surface parametrized by the elevation function $h(x, y)$. This flow is a superposition of internal waves with frequencies that are multiples of ω_0 , and a

wavelength matching that of the topographic feature that excites them. The flow exerts a pressure drag on a patch of surface, A is then equal to:

$$\mathcal{F} = \frac{1}{A} \int_A p \nabla h \, dx dy, \quad (6)$$

where p is the fluid's pressure at the surface.

Bell's original derivation made use of the traditional approximation, neglecting the vertical component of the Coriolis force, as is justified in the context of this original study focusing on the deep oceans. In order to apply the theory to the Earth's CMB, we have extended the formalism beyond that approximation. The resulting form drag can be found in the SI. The associated power flux writes:

$$\bar{\mathcal{P}} = \frac{\rho}{2\pi^2} \sum_{n=1}^{\infty} (n\omega_0) \int d^2k \frac{|\hat{h}|^2}{k} J_n(\beta)^2 \sqrt{(n^2\omega_0^2 - N^2)(f^2 - n^2\omega_0^2) + n^2\omega_0^2 f_s^2}, \quad (7)$$

where ρ is the density of the fluid, \hat{h} is the Fourier transform of h , $f = 2\Omega \sin \vartheta$ is the *Coriolis parameter*, and $f_s = 2\Omega \cos \vartheta \sin \alpha$, with α representing the angle between the direction of propagation of the wave, and the zonal direction. A determining parameter of the model is the combination: $\beta = U_0 k / \omega_0$, which measures the ratio between the tidal excursion and the topographic wavelength⁴⁸ $\sim k^{-1}$. For $\beta \ll 1$, the solution simplifies under the so-called *quasi-static approximation* (see Supplementary Information). The nutation theory gives $U_0 = 8.7 \times 10^{-5} \text{ m s}^{-1}$ at the CMB, and the tidal frequency is quasi-diurnal: $|\omega_0| \approx \Omega = 7.27 \times 10^{-5} \text{ s}^{-1}$. This gives $U_0/|\omega_0| \approx 1 \text{ m}$, and the quasi-static approximation is therefore well justified for topographic features wider than this length scale. Under that approximation, The sum in Equation (7) reduces to its first term, and the Bessel function $J_n(\beta)$ to the first term of its Taylor expansion.

Finally, we compute the total power transferred from the tidal flow to the internal waves

by integrating over the CMB surface:

$$\bar{P} = R^2 \int_0^{2\pi} d\varphi \int_{-\pi/2}^{\pi/2} d\vartheta \cos \vartheta \bar{\mathcal{P}}, \quad (8)$$

where R is the CMB radius. Likewise, we compute the equatorial torque in the format adequate for comparison with the nutation theory¹⁵ by combining the zonal and meridional components of the form drag and integrating over the CMB:

$$\tilde{\Gamma} = -R^3 \int_0^{2\pi} d\varphi \int_{-\pi/2}^{\pi/2} d\vartheta \cos \vartheta (\mathcal{F}_x \sin \vartheta + i\mathcal{F}_y) e^{i\varphi}. \quad (9)$$

Both integrations are carried out numerically to produce Figures 3 and ??, assuming the topographic power spectrum given in Equation (1).

References

- [1] V. Dehant and P. M. Mathews. *Precession, Nutation and Wobble of the Earth*. Cambridge University Press, Cambridge, 2015. ISBN 978-1-107-09254-9. doi: 10.1017/CBO9781316136133.
- [2] P. M. Mathews, T. A. Herring, and B. A. Buffett. Modeling of nutation and precession: New nutation series for nonrigid Earth and insights into the Earth's interior: NEW NUTATION SERIES AND THE EARTH'S INTERIOR. *Journal of Geophysical Research: Solid Earth*, 107(B4):ETG 3–1–ETG 3–26, April 2002. ISSN 01480227. doi: 10.1029/2001JB000390.
- [3] Bruce A. Buffett. Constraints on magnetic energy and mantle conductivity from the forced nutations of the Earth. *Journal of Geophysical Research*, 97(B13):19581, 1992. ISSN 0148-0227. doi: 10.1029/92JB00977.
- [4] B. A. Buffett, P. M. Mathews, and T. A. Herring. Modeling of nutation and precession:

Effects of electromagnetic coupling. *Journal of Geophysical Research: Solid Earth*, 107 (B4):ETG 5–1–ETG 5–14, April 2002. ISSN 01480227. doi: 10.1029/2000JB000056.

[5] P. M. Mathews and J. Y. Guo. Viscoelectromagnetic coupling in precession-nutation theory. *Journal of Geophysical Research: Solid Earth*, 110(B2), February 2005. ISSN 01480227. doi: 10.1029/2003JB002915.

[6] L. Koot, M. Dumberry, A. Rivoldini, O. De Viron, and V. Dehant. Constraints on the coupling at the core–mantle and inner core boundaries inferred from nutation observations. *Geophysical Journal International*, 182(3):1279–1294, 2010. ISSN 0956-540X. doi: 10.1111/j.1365-246X.2010.04711.x.

[7] T. H. Bell. Lee waves in stratified flows with simple harmonic time dependence. *Journal of Fluid Mechanics*, 67:705–722, February 1975. ISSN 0022-1120. doi: 10.1017/S0022112075000560.

[8] T. H. Bell. Topographically generated internal waves in the open ocean. *Journal of Geophysical Research*, 80(3):320–327, January 1975. ISSN 01480227. doi: 10.1029/JC080i003p00320.

[9] J. Vondrák and C. Ron. New method for determining free core nutation parameters, considering geophysical effects. *Astronomy & Astrophysics*, 604:A56, August 2017. ISSN 0004-6361, 1432-0746. doi: 10.1051/0004-6361/201730635.

[10] I Nurul Huda, S Lambert, C Bizouard, and Y Ziegler. Nutation terms adjustment to VLBI and implication for the Earth rotation resonance parameters. *Geophysical Journal International*, 220(2):759–767, February 2020. ISSN 0956-540X, 1365-246X. doi: 10.1093/gji/ggz468.

[11] Ping Zhu, Santiago A. Triana, Jérémie Rekier, Antony Trinh, and Véronique Dehant. Quantification of corrections for the main lunisolar nutation components and analysis

of the free core nutation from VLBI-observed nutation residuals. *Journal of Geodesy*, 123, 2021. ISSN 1432-1394. doi: 10.1007/s00190-021-01513-9.

[12] Huifeng Zhang and Wenbin Shen. Core–mantle topographic coupling: A parametric approach and implications for the formulation of a triaxial three-layered Earth rotation. *Geophysical Journal International*, 225(3):2060–2074, March 2021. ISSN 0956-540X, 1365-246X. doi: 10.1093/gji/ggab079.

[13] Bruce A. Buffett. Chemical stratification at the top of Earth’s core: Constraints from observations of nutations. *Earth and Planetary Science Letters*, 296(3-4):367–372, August 2010. ISSN 0012821X. doi: 10.1016/j.epsl.2010.05.020.

[14] J.A. Tyburczy and W.L. Du Frane. 2.25 - properties of rocks and minerals – the electrical conductivity of rocks, minerals, and the earth. In Gerald Schubert, editor, *Treatise on Geophysics (Second Edition)*, pages 661–672. Elsevier, Oxford, second edition edition, 2015. ISBN 978-0-444-53803-1. doi: 10.1016/B978-0-444-53802-4.00049-X.

[15] Jérémie Rekier. Free Core Nutation and Its Relation to the Spin-over Mode. *The Planetary Science Journal*, 3(6):133, June 2022. ISSN 2632-3338. doi: 10.3847/PSJ/ac6ce2.

[16] P. Olson. Core Dynamics: An Introduction and Overview. In *Treatise on Geophysics*, pages 1–25. Elsevier, 2015. ISBN 978-0-444-53803-1. doi: 10.1016/B978-0-444-53802-4.00137-8.

[17] Ankit Barik and Regupathi Angappan. planetMagFields: A Python package for analyzing andplotting planetary magnetic field data. *Journal of Open Source Software*, 9(97):6677, May 2024. ISSN 2475-9066. doi: 10.21105/joss.06677.

[18] P. Alken, E. Thébault, C. D. Beggan, H. Amit, J. Aubert, J. Baerenzung, T. N. Bondar, W. J. Brown, S. Califf, A. Chambodut, A. Chulliat, G. A. Cox, C. C. Finlay, A. Fournier, N. Gillet, A. Grayver, M. D. Hammer, M. Holschneider, L. Huder,

G. Hulot, T. Jager, C. Kloss, M. Korte, W. Kuang, A. Kuvshinov, B. Langlais, J.-M. Léger, V. Lesur, P. W. Livermore, F. J. Lowes, S. Macmillan, W. Magnes, M. Mandea, S. Marsal, J. Matzka, M. C. Metman, T. Minami, A. Morschhauser, J. E. Mound, M. Nair, S. Nakano, N. Olsen, F. J. Pavón-Carrasco, V. G. Petrov, G. Ropp, M. Rother, T. J. Sabaka, S. Sanchez, D. Saturnino, N. R. Schnepf, X. Shen, C. Stolle, A. Tangborn, L. Tøffner-Clausen, H. Toh, J. M. Torta, J. Varner, F. Vervelidou, P. Vigneron, I. Wardinski, J. Wicht, A. Woods, Y. Yang, Z. Zeren, and B. Zhou. International Geomagnetic Reference Field: The thirteenth generation. *Earth, Planets and Space*, 73(1):49, February 2021. ISSN 1880-5981. doi: 10.1186/s40623-020-01288-x.

[19] S. I. Braginsky. MAC-Oscillations of the Hidden Ocean of the Core. *Journal of geomagnetism and geoelectricity*, 45(11-12):1517–1538, 1993. doi: 10.5636/jgg.45.1517.

[20] Stanislav I. Braginsky. Dynamics of the stably stratified ocean at the top of the core. *Physics of the Earth and Planetary Interiors*, 111(1):21–34, February 1999. ISSN 0031-9201. doi: 10.1016/S0031-9201(98)00143-5.

[21] G. Higgins and G. C. Kennedy. The adiabatic gradient and the melting point gradient in the core of the Earth. *Journal of Geophysical Research (1896-1977)*, 76(8):1870–1878, 1971. ISSN 2156-2202. doi: 10.1029/JB076i008p01870.

[22] K. A. Whaler. Does the whole of the Earth’s core convect? *Nature*, 287(5782):528–530, October 1980. ISSN 1476-4687. doi: 10.1038/287528a0.

[23] David Gubbins. Geomagnetic constraints on stratification at the top of Earth’s core. *Earth, Planets and Space*, 59(7):661–664, July 2007. ISSN 1880-5981. doi: 10.1186/BF03352728. URL <https://doi.org/10.1186/BF03352728>.

[24] Bruce Buffett. Geomagnetic fluctuations reveal stable stratification at the top of the Earth’s core. *Nature*, 507(7493):484–487, March 2014. ISSN 1476-4687. doi:

10.1038/nature13122. URL <https://www.nature.com/articles/nature13122>. Publisher: Nature Publishing Group.

[25] Satoru Tanaka and Hiroyuki Hamaguchi. Velocities and Chemical Stratification in the Outermost Core. *Journal of geomagnetism and geoelectricity*, 45(11-12):1287–1301, 1993. doi: 10.5636/jgg.45.1287.

[26] George Helffrich and Satoshi Kaneshima. Causes and consequences of outer core stratification. *Physics of the Earth and Planetary Interiors*, 223:2–7, October 2013. ISSN 00319201. doi: 10.1016/j.pepi.2013.07.005.

[27] Satoshi Kaneshima. Array analyses of SmKS waves and the stratification of Earth’s outermost core. *Physics of the Earth and Planetary Interiors*, 276:234–246, March 2018. ISSN 00319201. doi: 10.1016/j.pepi.2017.03.006.

[28] Vivian Tang, Li Zhao, and Shu-Huei Hung. Seismological evidence for a non-monotonic velocity gradient in the topmost outer core. *Scientific Reports*, 5(1):8613, February 2015. ISSN 2045-2322. doi: 10.1038/srep08613.

[29] John R. Lister and Bruce A. Buffett. Stratification of the outer core at the core–mantle boundary. *Physics of the Earth and Planetary Interiors*, 105(1-2):5–19, January 1998. ISSN 00319201. doi: 10.1016/S0031-9201(97)00082-4. URL <https://linkinghub.elsevier.com/retrieve/pii/S0031920197000824>.

[30] D. Gubbins and C. J. Davies. The stratified layer at the core–mantle boundary caused by barodiffusion of oxygen, sulphur and silicon. *Physics of the Earth and Planetary Interiors*, 215:21–28, February 2013. ISSN 0031-9201. doi: 10.1016/j.pepi.2012.11.001.

[31] Jon Mound, Chris Davies, Sebastian Rost, and Jon Aurnou. Regional stratification at the top of Earth’s core due to core–mantle boundary heat flux variations. *Nature Geoscience*, 12(7):575–580, July 2019. ISSN 1752-0894, 1752-0908. doi: 10.1038/s41561-019-0381-z.

[32] Ur Christensen. Geodynamo models with a stable layer and heterogeneous heat flow at the top of the core. *Geophysical Journal International*, 215(2):1338–1351, November 2018. ISSN 0956-540X, 1365-246X. doi: 10.1093/gji/ggy352.

[33] Thomas Gastine, Julien Aubert, and Alexandre Fournier. Dynamo-based limit to the extent of a stable layer atop Earth’s core. *Geophysical Journal International*, 222(2):1433–1448, August 2020. ISSN 0956-540X. doi: 10.1093/gji/ggaa250.

[34] Julien Aubert. Rapid geomagnetic variations and stable stratification at the top of Earth’s core. *Physics of the Earth and Planetary Interiors*, 362:107335, May 2025. ISSN 0031-9201. doi: 10.1016/j.pepi.2025.107335.

[35] Paula Koelemeijer. Toward Consistent Seismological Models of the Core–Mantle Boundary Landscape. In Hauke Marquardt, Maxim Ballmer, Sanne Cottaar, and Jasper Konter, editors, *Geophysical Monograph Series*, pages 229–255. Wiley, 1 edition, July 2021. ISBN 978-1-119-52861-6 978-1-119-52860-9. doi: 10.1002/9781119528609.ch9.

[36] Björn H. Heyn, Clinton P. Conrad, and Reidar G. Trønnes. Core-mantle boundary topography and its relation to the viscosity structure of the lowermost mantle. *Earth and Planetary Science Letters*, 543:116358, August 2020. ISSN 0012821X. doi: 10.1016/j.epsl.2020.116358.

[37] J.-S. Gagnon, S. Lovejoy, and D. Schertzer. Multifractal earth topography. *Nonlinear Processes in Geophysics*, 13(5):541–570, October 2006. ISSN 1607-7946. doi: 10.5194/npg-13-541-2006.

[38] Thibault Candela, François Renard, Yann Klinger, Karen Mair, Jean Schmittbuhl, and Emily E. Brodsky. Roughness of fault surfaces over nine decades of length scales. *Journal of Geophysical Research: Solid Earth*, 117(B8):2011JB009041, August 2012. ISSN 0148-0227. doi: 10.1029/2011JB009041.

[39] Alberto C. Naveira Garabato, A. J. George Nurser, Robert B. Scott, and John A. Goff. The Impact of Small-Scale Topography on the Dynamical Balance of the Ocean. *Journal of Physical Oceanography*, 43(3):647–668, March 2013. ISSN 0022-3670, 1520-0485. doi: 10.1175/JPO-D-12-056.1.

[40] B. N. J. Persson, O. Albohr, U. Tartaglino, A. I. Volokitin, and E. Tosatti. On the nature of surface roughness with application to contact mechanics, sealing, rubber friction and adhesion. *Journal of Physics: Condensed Matter*, 17(1):R1, December 2004. ISSN 0953-8984. doi: 10.1088/0953-8984/17/1/R01.

[41] Tevis D B Jacobs, Till Junge, and Lars Pastewka. Quantitative characterization of surface topography using spectral analysis. *Surface Topography: Metrology and Properties*, 5(1):013001, January 2017. ISSN 2051-672X. doi: 10.1088/2051-672X/aa51f8.

[42] N. Rodriguez, L. Gontard, C. Ma, R. Xu, and B. N. J. Persson. On How to Determine Surface Roughness Power Spectra. *Tribology Letters*, 73(1):18, March 2025. ISSN 1023-8883, 1573-2711. doi: 10.1007/s11249-024-01933-6.

[43] Geoffrey K Vallis. *Atmospheric and oceanic fluid dynamics*. Cambridge University Press, 2017.

[44] Stefan G Llewellyn Smith and WR Young. Conversion of the barotropic tide. *Journal of Physical Oceanography*, 32(5):1554–1566, 2002.

[45] Jérémie Rekier, Benjamin F. Chao, Jianli Chen, Véronique Dehant, Séverine Rosat, and Ping Zhu. Earth’s Rotation: Observations and Relation to Deep Interior. *Surveys in Geophysics*, 43(1):149–175, November 2021. ISSN 1573-0956. doi: 10.1007/s10712-021-09669-x.

[46] B A Buffett. Conditions for turbulent Ekman layers in precessionally driven flow. *Geophysical Journal International*, 226(1):56–65, 2021. ISSN 0956-540X. doi: 10.1093/gji/ggab088.

[47] Sheng-An Shih, Santiago Andrés Triana, Jérémie Rekier, and Véronique Dehant. Turbulent dissipation in the boundary layer of precession-driven flow in a sphere. *AIP Advances*, 13(7):075025, July 2023. ISSN 2158-3226. doi: 10.1063/5.0146932.

[48] Chris Garrett and Eric Kunze. Internal Tide Generation in the Deep Ocean. *Annual Review of Fluid Mechanics*, 39(1):57–87, January 2007. ISSN 0066-4189, 1545-4479. doi: 10.1146/annurev.fluid.39.050905.110227.

Data availability

The JUPYTER notebooks used to generate the Figures 1, 3, and 4, have been made publicly available via the following repository: <https://doi.org/10.5281/zenodo.15748778>.

Acknowledgments

The research leading to these results has received funding from the European Research Council (ERC) under the European Union’s Horizon 2020 research and innovation program (Synergy Grant 855677 GRACEFUL). D.A. acknowledges support from the U.S. Department of Energy, Office of Science, Office of Advanced Scientific Computing Research, Department of Energy Computational Science Graduate Fellowship Award Number (DE-SC0023112).

Author Contributions

J.R. conceptualized and directed the study and derived the main results. S. A. T., A. B., D. A., and W. K. contributed to building the mathematical framework and to the writing of the manuscript.

Competing Interests

The authors declare no competing interests.

Supplementary information to *Constraints on Earth's Core-Mantle boundary from nutation*

J. Rekier^{1*}, S. A. Triana¹, A. Barik², D. Abdulah³, W. Kang³

¹Royal Observatory of Belgium, 3 avenue circulaire, 1180 Brussels, Belgium

²Johns Hopkins University, 3400 North Charles Street, Baltimore, MD 21218, USA

³Earth, Atmospheric and Planetary Science, Massachusetts Institute of Technology, USA

*Corresponding author. Email: jeremy.rekier@observatory.be.

July 14, 2025

1 Governing equations and solution

We look at an oscillating flow over a rough surface with a topography represented by the elevation function: $h(x, y)$. Bell (1975) gave the boundary condition for this problem as¹:

$$w|_{z=0} = \mathbf{U} \cdot \nabla h, \quad (1)$$

where w is the vertical velocity, and \mathbf{U} is the background flow. Following Bell², we introduce the horizontal coordinates vector in a moving frame where the base flow appears at rest:

$$\boldsymbol{\xi} \equiv \mathbf{x} - \int_0^t \mathbf{U}(\tau) d\tau, \quad (2)$$

where $\mathbf{x}^\top = (x, y)$ is the horizontal position vector in the rest frame. The vertical velocity may be decomposed into Fourier modes in either frames:

$$w = \frac{1}{4\pi^2} \int d^2k \hat{w} e^{i\mathbf{k}\cdot\mathbf{x}} = \frac{1}{4\pi^2} \int d^2k \tilde{w} e^{i\mathbf{k}\cdot\boldsymbol{\xi}}, \quad (3)$$

from which we deduce the relation between a Fourier component in the rest frame, \hat{w} , and in the moving frame, \tilde{w} :

$$\hat{w} = \tilde{w} e^{-i\mathbf{k}\cdot\int_0^t \mathbf{U}(\tau) d\tau}. \quad (4)$$

Injecting into the boundary condition (1) yields:

$$\begin{aligned} w|_{z=0} &= \mathbf{U} \cdot \nabla h \\ \leftrightarrow \tilde{w}_0 &= i(\mathbf{k} \cdot \mathbf{U}) \hat{h} e^{i\mathbf{k}\cdot\int_0^t d\tau \mathbf{U}(\tau)} \\ \leftrightarrow \tilde{w}_0 &= \hat{h} \frac{d}{dt} e^{i\mathbf{k}\cdot\int_0^t d\tau \mathbf{U}(\tau)}, \end{aligned} \quad (5)$$

where $\hat{w}_0 \equiv \hat{w}_{z=0}$, and likewise for \tilde{w} . Bell examined the one-dimensional harmonic forcing. We are interested in the tidal flow produced by a single retrograde nutation component, which can be written as³:

$$\mathbf{U} = U_x \cos(\omega_0 t + \varphi) \hat{\mathbf{x}} - U_y \sin(\omega_0 t + \varphi) \hat{\mathbf{y}}, \quad (6)$$

where $\hat{\mathbf{x}}$, and $\hat{\mathbf{y}}$, are unit vectors along the zonal and meridional directions, respectively (see Fig. 1). From equation (6), we compute the argument of the exponential in equation (5):

$$\begin{aligned} \mathbf{k} \cdot \int_0^t d\tau \mathbf{U}(\tau) &= \frac{k_x U_x}{\omega_0} (\sin(\omega_0 t + \varphi) - \sin \varphi) + \frac{k_y U_y}{\omega_0} (\cos(\omega_0 t + \varphi) - \cos \varphi) \\ &= \beta \sin(\omega_0 t + \varphi + \gamma) - \beta \sin(\varphi + \gamma), \end{aligned} \quad (7)$$

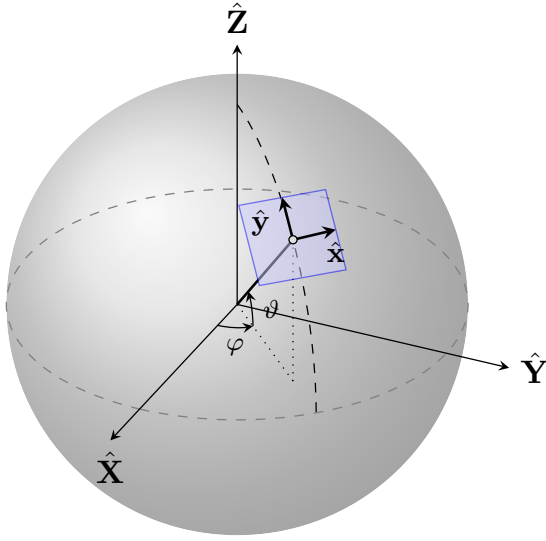


Figure 1: Local basis vectors and terrestrial coordinates definition. ϑ is the Earth's latitude, and φ is the longitude.

where we have defined:

$$\beta = \sqrt{\frac{k_x^2 U_x^2 + k_y^2 U_y^2}{\omega_0^2}}, \quad \gamma = \arctan\left(\frac{k_y U_y}{k_x U_x}\right). \quad (8)$$

In what follows it will be useful to define the polar coordinates in Fourier space:

$$\begin{cases} k_x = k \cos \alpha, \\ k_y = k \sin \alpha. \end{cases} \quad (9)$$

Following Bell¹, we apply the Jacobi-Anger relation to the boundary condition and find:

$$\tilde{w}_0 = \hat{h} \sum_{n=-\infty}^{\infty} J_n(\beta) (in\omega_0) e^{in\omega_0 t} e^{in(\varphi+\gamma)} e^{-i\beta \sin(\varphi+\gamma)}. \quad (10)$$

Note the awkward trailing constant phase factor which can't be avoided but proves harmless (see below). From equation (10), we can guess that the oscillation of the tidal flow over the topography at the frequency ω_0 generates waves at the same frequency as well as higher

harmonics.

The dynamics of each individual wave is governed by the momentum, buoyancy, and incompressibility equations:

$$\frac{Du}{Dt} + \tilde{f}w - fv = -\frac{1}{\rho} \frac{\partial p}{\partial x} \quad (11a)$$

$$\frac{Dv}{Dt} + fu = -\frac{1}{\rho} \frac{\partial p}{\partial y} \quad (11b)$$

$$\frac{Dw}{Dt} - \tilde{f}u = -\frac{1}{\rho} \frac{\partial p}{\partial z} + b \quad (11c)$$

$$\frac{Db}{Dt} = -N^2 w \quad (11d)$$

$$\frac{\partial u}{\partial x} + \frac{\partial v}{\partial y} + \frac{\partial w}{\partial z} = 0 \quad (11e)$$

where $f = 2\Omega \sin \vartheta$, and $\tilde{f} = 2\Omega \cos \vartheta$, with ϑ denoting latitude, and Ω the Earth's spin rate.

To linear order in the velocity, the material derivative reduces to:

$$\frac{D}{Dt} \equiv \left(\frac{\partial}{\partial t} + \mathbf{U} \cdot \nabla \right), \quad (12)$$

which corresponds to the time derivative in the moving frame defined by equation (2).

Equations (11a) to (11e) can be combined into a single equation for w :

$$\left(\frac{D^2}{Dt^2} \nabla^2 + (\mathbf{f} \cdot \nabla)^2 + N^2 \nabla_h^2 \right) w = 0, \quad (13)$$

where $\mathbf{f}^\tau = (0, \tilde{f}, f)$, and $\nabla_h^2 = \left(\frac{\partial^2}{\partial x^2} + \frac{\partial^2}{\partial y^2} \right)$. Based on (10), we expect the solution to be a superposition of harmonic functions of the form:

$$\tilde{w} = \sum_{n=-\infty}^{\infty} \tilde{w}^{(n)} e^{in\omega_0 t}. \quad (14)$$

In Fourier space, equation (13) applied to individual harmonics becomes:

$$\left(\underbrace{(f^2 - n^2 \omega_0^2)}_A \frac{d^2}{dz^2} + \underbrace{2ikff_s}_{2iB} \frac{d}{dz} + \underbrace{(n^2 \omega_0^2 - N^2 - f_s^2)k^2}_C \right) \tilde{w}^{(n)} = 0, \quad (15)$$

where we have used (9), and we have defined $f_s = \tilde{f} \sin \alpha$. Inspired by Gerkema and Zimmerman⁴, we guess the following solution:

$$\tilde{w}^{(n)} = \tilde{w}_0^{(n)} e^{imz}, \quad (16)$$

where the vertical wave number is defined as:

$$m = \pm \sqrt{\frac{CA + B^2}{A^2} - \frac{B}{A}} \\ \leftrightarrow m = \frac{k}{(f^2 - n^2 \omega_0^2)} \left(-\text{sgn}(n) \sqrt{(n^2 \omega_0^2 - N^2)(f^2 - n^2 \omega_0^2) + n^2 \omega_0^2 f_s^2} - ff_s \right) \quad (17)$$

where we have inserted $-\text{sgn}(n)$ to ensure downward energy propagation¹.

It will be essential to have expressions for the horizontal components of the velocity, and pressure. These will have a plane wave form analogous to equation (16) and can be recovered from equations (11a) to (11e) in Fourier space:

$$in\omega_0 \tilde{u}_0^{(n)} - f \tilde{v}_0^{(n)} + \tilde{f} \tilde{w}_0^{(n)} = -\frac{ik}{\rho} \cos \alpha \tilde{p}_0^{(n)} \quad (18a)$$

$$in\omega_0 \tilde{v}_0^{(n)} + f \tilde{u}_0^{(n)} = -\frac{ik}{\rho} \sin \alpha \tilde{p}_0^{(n)} \quad (18b)$$

$$in\omega_0 \tilde{w}_0^{(n)} - \tilde{f} \tilde{v}_0^{(n)} = -\frac{i}{\rho} m \tilde{p}_0^{(n)} + \tilde{b}_0^{(n)} \quad (18c)$$

$$in\omega_0 \tilde{b}_0^{(n)} + N^2 \tilde{w}_0^{(n)} = 0 \quad (18d)$$

$$ik(\tilde{u}_0^{(n)} \cos \alpha + \tilde{v}_0^{(n)} \sin \alpha) = -im \tilde{w}_0^{(n)}. \quad (18e)$$

We are mostly interested in the pressure coefficient, which proves to be:

$$\begin{aligned}\tilde{p}_0^{(n)} &= \frac{\rho}{n\omega_0 k^2} (n^2\omega_0^2 - f^2) m\tilde{w}_0^{(n)} - \frac{\rho f f_s}{n\omega_0 k} \tilde{w}_0^{(n)} + i \frac{\rho f_c}{k} \tilde{w}_0^{(n)} \\ &= \text{sgn}(n) \frac{\rho}{n\omega_0 k} \sqrt{(n^2\omega_0^2 - N^2)(f^2 - n^2\omega_0^2) + n^2\omega_0^2 f_s^2} \tilde{w}_0^{(n)} + i \frac{\rho f_c}{k} \tilde{w}_0^{(n)}\end{aligned}\quad (19)$$

where $f_c = \tilde{f} \cos \alpha$.

2 Form drag

The average pressure drag on a surface of area, A of the boundary is:

$$\mathcal{F} = \frac{1}{A} \int_A d^2x \ p|_{z=0} \nabla h. \quad (20)$$

The integrand is a real quantity. Upon changing to the base flow coordinates eq. (2) and using the Fourier transform eq. (3), we get:

$$\begin{aligned}\mathcal{F} &= \frac{1}{A} \int_A d^2\xi \ p^*|_{z=0} \nabla h \\ &= \frac{1}{(4\pi^2)^2} \int d^2k \ (i\mathbf{k}) \int d^2k' \ \tilde{p}_0(\mathbf{k}')^* \tilde{h}(\mathbf{k}) \underbrace{\frac{1}{A} \int_A d^2\xi e^{i(\mathbf{k}-\mathbf{k}') \cdot \xi}}_{4\pi^2 A \delta(\mathbf{k}-\mathbf{k}')} \\ &= \frac{1}{4\pi^2} \int d^2k \ (i\mathbf{k}) \ \tilde{p}_0(\mathbf{k})^* \tilde{h}(\mathbf{k}) \\ &= \frac{1}{4\pi^2} \int d^2k \ (i\mathbf{k}) \ \tilde{p}_0(\mathbf{k})^* \hat{h}(\mathbf{k}) e^{i\mathbf{k} \cdot \int_0^t \mathbf{U}(\tau) d\tau},\end{aligned}\quad (21)$$

where we have assumed that the average is done over a sufficiently wide surface, A , justifying the identification in the under brace on the second line. Using the Jacobi-Anger identity again:

$$e^{i\mathbf{k} \cdot \int_0^t d\tau \mathbf{U}(\tau)} = \sum_{n=-\infty}^{\infty} J_n(\beta) e^{in\omega_0 t} e^{in(\varphi+\gamma)} e^{-i\beta \sin(\varphi+\gamma)}. \quad (22)$$

Inserting back into equation (21) yields:

$$\mathcal{F} = \frac{\rho}{4\pi^2} \sum_{n=-\infty}^{\infty} \sum_{m=-\infty}^{\infty} \int d^2k \frac{|\hat{h}|^2}{k} J_n(\beta) J_m(\beta) \mathcal{M}_n e^{i(n-m)(\omega_0 t + \phi + \gamma)}, \quad (23)$$

with \mathcal{M}_n read from equation (19):

$$\mathcal{M}_n = \text{sgn}(n) \sqrt{(n^2\omega_0^2 - N^2)(f^2 - n^2\omega_0^2) + n^2\omega_0^2 f_s^2} + i n \omega_0 f_c. \quad (24)$$

Using the fact that \mathcal{F} is a real quantity, we finally obtain:

$$\begin{aligned} \mathcal{F} = & -\frac{\rho}{4\pi^2} \sum_{n=-\infty}^{\infty} \sum_{m=-\infty}^{\infty} \int d^2k \frac{|\hat{h}|^2}{k} J_n(\beta) J_m(\beta) \\ & \times \left(\text{sgn}(n) \sqrt{(n^2\omega_0^2 - N^2)(f^2 - n^2\omega_0^2) + n^2\omega_0^2 f_s^2} \cos((n-m)(\omega_0 t + \phi + \gamma)) \right. \\ & \quad \left. + n \omega_0 f_c \sin((n-m)(\omega_0 t + \phi + \gamma)) \right). \end{aligned} \quad (25)$$

Let's focus on the second term in the parentheses which has the structure:

$$\begin{aligned} \sum_{n=-\infty}^{\infty} \sum_{m=-\infty}^{\infty} n J_n(\beta) J_m(\beta) \sin((n-m)(\omega_0 t + \varphi + \gamma)) &= \sum_{l=-\infty}^{\infty} \underbrace{\sin(l(\omega_0 t + \varphi + \gamma))}_{l\beta/2} \sum_{n=-\infty}^{\infty} n J_n(\beta) J_{n-l}(\beta) \\ &= \frac{\beta}{2} \sum_{l=-\infty}^{\infty} l \sin(l(\omega_0 t + \varphi + \gamma)). \end{aligned} \quad (26)$$

The resulting series evaluates to zero in the distributional sense. The final expression is thus:

$$\begin{aligned} \mathcal{F} = & -\frac{\rho}{4\pi^2} \sum_{n=-\infty}^{\infty} \sum_{m=-\infty}^{\infty} \int d^2k \frac{|\hat{h}|^2}{k} J_n(\beta) J_m(\beta) \\ & \text{sgn}(n) \sqrt{(n^2\omega_0^2 - N^2)(f^2 - n^2\omega_0^2) + n^2\omega_0^2 f_s^2} \cos((n-m)(\omega_0 t + \varphi + \gamma)). \end{aligned} \quad (27)$$

3 Power flux

We can arrive at a simple expression for the power flux by taking the dot product of equation (20) with the base flow. Using the boundary condition equation (1) gives:

$$\begin{aligned}\mathcal{P} &= \frac{1}{A} \int_A d^2\xi \ p^*|_{z=0} (\mathbf{U} \cdot \nabla h) \\ &= \frac{1}{A} \int_A d^2\xi \ p^* w|_{z=0}.\end{aligned}\quad (28)$$

The average power flux over the fundamental period is then:

$$\begin{aligned}\bar{\mathcal{P}} &= \frac{\omega_0}{2\pi} \int_0^{2\pi/\omega_0} dt \ \frac{1}{A} \int_A d^2\xi \ p^* w|_{z=0} \\ &= \frac{\omega_0}{2\pi} \frac{1}{4\pi^2} \int_0^{2\pi/\omega_0} dt \int d^2k \ \frac{1}{2} (\tilde{p}_0^* \tilde{w}_0 + \tilde{p}_0 \tilde{w}_0^*).\end{aligned}\quad (29)$$

Focusing on the second term in the parentheses and using equations (10) and (19):

$$\begin{aligned}\int_0^{2\pi/\omega_0} dt \ \tilde{w}_0^* \tilde{p}_0 &= \sum_{n=-\infty}^{\infty} \sum_{m=-\infty}^{\infty} \frac{\rho}{k} (m\omega_0) \left(\sqrt{(m^2\omega_0^2 - N^2)(f^2 - m^2\omega_0^2) + m^2\omega_0^2 f_s^2} + im\omega_0 f_c \right) \\ &\quad \times \text{sgn}(m) J_n^*(\beta) J_m(\beta) e^{i(m-n)\gamma} \underbrace{\int_0^{2\pi/\omega_0} dt \ e^{i(m-n)\omega_0 t}}_{(2\pi/\omega_0)\delta_{n,m}}.\end{aligned}\quad (30)$$

Adding up the other term, when the dust settles, we get:

$$\bar{\mathcal{P}} = \frac{\rho}{2\pi^2} \sum_{n=1}^{\infty} (n\omega_0) \int d^2k \frac{|\hat{h}|^2}{k} J_n(\beta)^2 \sqrt{(n^2\omega_0^2 - N^2)(f^2 - n^2\omega_0^2) + n^2\omega_0^2 f_s^2}, \quad (31)$$

which generalizes the expression found by² under the traditional approximation.

4 Quasi-static approximation

If $\beta \sim U k / \omega_0$ is small, the terms in equation (27) for which $n = \pm 1$ and $m = 0$ dominate the double sum. This is the so called *quasi-static* approximation, under which the form drag reduces to:

$$\mathcal{F} \approx -\frac{\rho}{2\pi^2} \int d^2 k \mathbf{k} \frac{|\hat{h}|^2}{k} J_1(\beta) J_0(\beta) \sqrt{(\omega_0^2 - N^2)(f^2 - \omega_0^2) + \omega_0^2 f_s^2} \cos(\omega_0 t + \varphi + \gamma). \quad (32)$$

Under the same approximation, the Bessel functions can be approximated as $J_n(\beta) \approx (\beta/2)^n / n!$.

The double integral can be advantageously evaluated in the polar coordinates defined by equation (9). Before doing so, it is helpful to linger a bit on the following product:

$$\sqrt{U_x^2 \cos^2 \alpha + U_y^2 \sin^2 \alpha} \cos(\omega_0 t + \varphi + \gamma) = (U_x \cos(\omega_0 t + \varphi) \cos \alpha - U_y \sin(\omega_0 t + \varphi) \sin \alpha), \quad (33)$$

where we used elementary trigonometric properties and the definition of γ given by equation (8). Using the above, the zonal and meridional components of the form drag are, respectively:

$$\mathcal{F}_x \approx -\frac{\rho U_x}{4\pi^2 |\omega_0|} \int_0^\infty dk k^2 \int_0^{2\pi} d\alpha |\hat{h}|^2 \sqrt{(\omega_0^2 - N^2)(f^2 - \omega_0^2) + \omega_0^2 f_s^2} \cos^2 \alpha \cos(\omega_0 t + \varphi), \quad (34)$$

$$\mathcal{F}_y \approx -\frac{\rho U_y}{4\pi^2 |\omega_0|} \int_0^\infty dk k^2 \int_0^{2\pi} d\alpha |\hat{h}|^2 \sqrt{(\omega_0^2 - N^2)(f^2 - \omega_0^2) + \omega_0^2 f_s^2} \sin^2 \alpha \sin(\omega_0 t + \varphi). \quad (35)$$

From equation (31), the power flux approximates to:

$$\bar{\mathcal{P}} \approx \frac{\rho}{8\pi^2 |\omega_0|} \int_0^\infty dk k^2 \int_0^{2\pi} d\alpha |\hat{h}|^2 (U_x^2 \cos^2 \alpha + U_y^2 \sin^2 \alpha) \sqrt{(\omega_0^2 - N^2)(f^2 - \omega_0^2) + \omega_0^2 f_s^2}. \quad (36)$$

5 Traditional approximation

Under the *traditional approximation*, one neglects the terms proportional to \tilde{f} in equations (11a) and (11c). To us, this amounts to set $f_s = 0$ in the equations for the form drag (34) and (35), and the power flux (36). Assuming that \hat{h} is isotropic, i.e. that it depends only on the norm of the wave vector, k , the integrals over α may be carried out simply, which yields:

$$\mathcal{F}_x \approx -\frac{\rho U_x}{4\pi|\omega_0|} \cos(\omega_0 t + \varphi) \sqrt{(\omega_0^2 - N^2)(f^2 - \omega_0^2)} \int_0^\infty dk k^2 |\hat{h}|^2, \quad (37)$$

$$\mathcal{F}_y \approx \frac{\rho U_x}{4\pi|\omega_0|} \sin(\omega_0 t + \varphi) \sqrt{(\omega_0^2 - N^2)(f^2 - \omega_0^2)} \int_0^\infty dk k^2 |\hat{h}|^2, \quad (38)$$

for the form drag, and:

$$\bar{\mathcal{P}} \approx \frac{\rho}{4\pi|\omega_0|} (U_x^2 + U_y^2) \sqrt{(\omega_0^2 - N^2)(f^2 - \omega_0^2)} \int_0^\infty dk k^2 |\hat{h}|^2, \quad (39)$$

for the average power flux.

6 Topographic power spectrum

The factor $|\hat{h}|^2$ appearing in equations (37) to (39) defines the *power spectrum* characterizing the surface topography which we have treated as isotropic. In what follows, we further assume a generic power spectrum of the form:

$$|\hat{h}|^2 = \begin{cases} \frac{h_{\text{rms}}^2 \mathcal{H}}{k_0^2 \pi} \left(\frac{k}{k_0}\right)^{-2(\mathcal{H}+1)} & k \geq k_0, \\ 0 & k < k_0, \end{cases} \quad (40)$$

where k_0 denotes a minimal cutoff scale, and \mathcal{H} is the *Hurst exponent* measuring the degree of fractality of the surface. The spectrum is normalized so that:

$$\begin{aligned} h_{\text{rms}}^2 &= \int d^2k |\hat{h}|^2 \\ &= \underbrace{\int_0^{2\pi} d\alpha}_{2\pi} \int_0^\infty dk k |\hat{h}|^2 \end{aligned} \quad (41)$$

where h_{rms} is the *root-mean-square* amplitude of the topography. The following integral therefore evaluates to:

$$\int_0^\infty dk k^2 |h|^2 = \frac{h_{\text{rms}}^2 k_0}{\pi} \frac{\mathcal{H}}{2\mathcal{H} - 1}. \quad (42)$$

7 Integrated power flux

We are interested in the total power dissipated by the tidal flow associated with the Earth's nutation. This tidal flow has the form:

$$\begin{cases} U_x = U_0 \sin \vartheta, \\ U_y = U_0, \end{cases} \quad (43)$$

where ϑ is the latitude and $U_0 = 8.7 \times 10^{-5} \text{ m/s}$. The frequency of the nutation is quasi-diurnal in the terrestrial reference frame: $|\omega_0| \approx \Omega = 7.27 \times 10^{-5} \text{ s}^{-1}$. We have $U_0/|\omega_0| \approx 1 \text{ m}$, so that the quasi-static approximation is well justified for topographic features wider than this length scale.

For this specific type of flow, the formula for the average power flux under the traditional approximation is analytical:

$$\bar{\mathcal{P}}_{\text{TA}} = \frac{\rho h_{\text{rms}}^2 k_0 U_0^2 \Omega}{4\pi^2} \frac{\mathcal{H}}{2\mathcal{H} - 1} \sqrt{\left(1 - \frac{N^2}{\Omega^2}\right) (4 \sin^2 \vartheta - 1) (1 + \sin^2 \vartheta)}. \quad (44)$$

From equation (44), we identify two regimes for which the square root is real valued. If

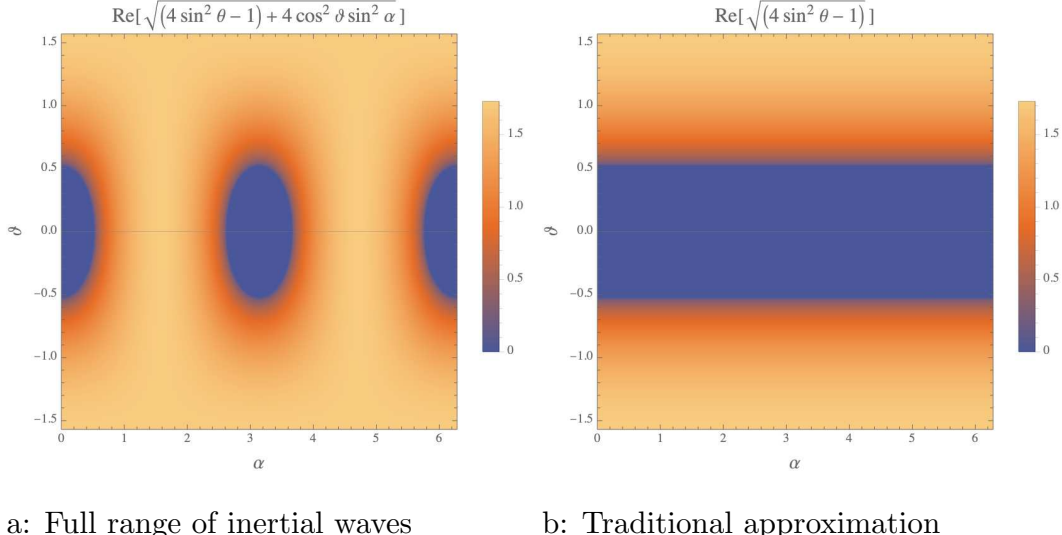


Figure 2: The traditional approximation artificially confines the inertial waves to polar caps corresponding to the latitudes $|\vartheta| > 30^\circ$.

$N > \Omega$, the power flux from the surface is caused by the excitation of gravity waves confined within the equatorial band $|\vartheta| \leq 30^\circ$. If $N < \Omega$, the power flux is caused by inertial waves confined to the polar caps $|\vartheta| \geq 30^\circ$. This confinement is, however, in large parts an artifact of using the traditional approximation. Reintroducing the term proportional to $f_s = 2\Omega \cos \vartheta \sin \alpha$ inside the square root extends the range of latitudes in the inertial waves regime as can be seen from Fig. 2. The reintroduction of this term must be carried out before performing the angular integration over α in equation (36), which must then be done numerically.

Once the power flux is known, the total power input into the topographic waves generated by the entire spherical surface of radius R is:

$$\bar{P} = R^2 \int_0^{2\pi} d\varphi \int_{-\pi/2}^{\pi/2} d\vartheta \cos \vartheta \bar{\mathcal{P}}. \quad (45)$$

In the traditional approximation, this gives:

$$\bar{P}_{\text{TA}} = \frac{\rho R^2 h_{\text{rms}}^2 k_0 U_0^2 \Omega}{8\pi^2} \frac{\mathcal{H}}{2\mathcal{H} - 1} \text{Re} \left[17\pi \sqrt{\frac{N^2}{\Omega^2} - 1} + 2\sqrt{1 - \frac{N^2}{\Omega^2}} \left(46\sqrt{3} - 17\log(2 + \sqrt{3}) \right) \right]. \quad (46)$$

References

- [1] T. H. Bell. Lee waves in stratified flows with simple harmonic time dependence. *Journal of Fluid Mechanics*, 67:705–722, February 1975. ISSN 0022-1120. doi: 10.1017/S0022112075000560.
- [2] T. H. Bell. Topographically generated internal waves in the open ocean. *Journal of Geophysical Research*, 80(3):320–327, January 1975. ISSN 01480227. doi: 10.1029/JC080i003p00320.
- [3] Sheng-An Shih, Santiago Andrés Triana, Jérémie Requier, and Véronique Dehant. Turbulent dissipation in the boundary layer of precession-driven flow in a sphere. *AIP Advances*, 13(7):075025, July 2023. ISSN 2158-3226. doi: 10.1063/5.0146932.
- [4] T Gerkema and J T F Zimmerman. Lecture Notes: An introduction to internal waves, 2008.